International Journal of Robotics and Control Systems
Vol. 5, No. 5, 2025, pp. 2469-2485
ISSN 2775-2658
http://pubs2.ascee.org/index.php/ijrcs

Center of Mass and Zero Moment Point Computation for Balance Identification of a Humanoid Robot using an Inertial Measurement Unit and Unscented Kalman Filtering

Gembong Edhi Setyawan [a,1], Edita Rosana Widasari [a,2,*], Syarifah Alexandria [a,3]

[a] Department of Informatics Engineering, Faculty of Computer Science, Universitas Brawijaya, Indonesia
[1] gembong@ub.ac.id; [2] editarosanaw@ub.ac.id; [3] syarifah.alex@student.ub.ac.id
* Corresponding Author

ARTICLE INFO

Article history
Received August 20, 2025
Revised September 30, 2025
Accepted November 18, 2025

Keywords
Center of Mass;
Humanoid robot;
Inertial Measurement Units;
Unscented Kalman Filter;
Zero Moment Point

ABSTRACT

Humanoid robots require advanced balance control systems to safely and efficiently operate in dynamic and unstructured environments. The research contribution is an IMU-only balance-detection framework introducing a quantitative Responsiveness Index (RI) to compare the responsiveness of Center of Mass (CoM) and model-based Zero Moment Point (ZMP) estimation. The proposed method integrates CoM and ZMP analyses derived exclusively from Inertial Measurement Unit (IMU) data and employs an Unscented Kalman Filter (UKF) with optimized parameters (α=0.10, β=2, process noise covariance Q = 0.10, measurement noise covariance R = 0.10) obtained through sensitivity analysis across multiple motion states. This configuration effectively suppresses IMU noise and stabilizes attitude estimation on the DARwIn-OP3 humanoid platform. Experimental validation showed that CoM estimation achieved accuracies of 85.71 % for x, 97.85 % for y, and 99.96 % for z relative to CAD-based static references, while ZMP estimation reached 71.43 % for x and 94.89 % for y, and the Support Polygon (SP) area matched the model within ± 0.5 %. The proposed RI metric revealed that ZMP detected balance transitions approximately 20 % faster than CoM during dynamic walking and kicking, confirming its superior responsiveness. These findings demonstrate that IMU-derived, model-based ZMP estimation provides an effective, real-time indicator of humanoid balance changes, enabling future development of closed-loop control strategies to maintain ZMP within the SP for improved dynamic stability.

1. Introduction

Balance and stability control are essential for the safe and effective operation of humanoid robots performing tasks in dynamic and unstructured environments [1], [2]. Applications include disaster response [3], [4], [5], industrial automation [6], personal assistance [7], [8], and healthcare [9], [10]. Even minor instability can compromise robot functionality and safety. The Center of Mass (CoM) and Zero Moment Point (ZMP) remain fundamental metrics in humanoid stability control. This research addresses a critical gap by providing a quantitative comparative analysis of CoM and ZMP responsiveness using an IMU-only framework, enabling real-time balance detection without external

force or vision sensors. However, IMU-based sensing also faces challenges such as drift accumulation and bias instability, which this study mitigates through optimized Unscented Kalman Filter (UKF) parameterization.

The concept of CoM, which is based on classical mechanics, is crucial for realizing the balance and motion of humanoid robots. The main challenge in using CoM for humanoid robot balance control is precisely estimating the robot's CoM [11]. The CoM is critical in determining the robot's stability, as it regulates its weight distribution and response to external forces. By accurately estimating CoM, the robot can anticipate and respond to disturbances, thereby ensuring stability. Various traditional methods have been employed to estimate CoM in humanoid robotics. One of the traditional methods for estimating CoM involves using force and torque sensors affixed to the soles [12], [13]. Although force and torque sensors are effective for static or quasi-static balance, they are not particularly effective in providing precise CoM data during rapid and dynamic movements, and they also add weight and complicate the robot's gears. An alternative traditional approach involves a vision-based system that examines body posture to estimate CoM using a camera [14]. The vision-based approach is highly practicable but is susceptible to lighting conditions and reliance on external infrastructure. In addition, kinematic models are a method for estimating CoM [15], [16], [17]. These kinematic models segment the robot body and employ joint angle information. Despite their technical feasibility, they frequently rely on rigid assumptions that disregard real-time, dynamic changes in weight distribution, particularly when the robot is in motion or under the influence of external factors.

Furthermore, ZMP provides a dynamic stability criterion that has been extensively implemented in both theoretical analysis and practical applications of humanoid robotics, such as WABOT from Waseda-Japan [11], [18], Honda's ASIMO [19], the HRP series [20], [21], and HUBO [22], [23]. The resultant moment of forces acting on the robot is zero at a point on the ground established by ZMP [24], [25], [26]. The robot's balance can be identified by monitoring the ZMP's position in relation to the robot's support polygon [27]. The practical implementation of ZMP in real-world scenarios presents many challenges. The challenges encompass the precise sensing and quantification of the forces at play and the real-time adaptation to dynamic changes in the robot's posture and external disturbances [28]. Additionally, ZMP-based methodologies frequently necessitate simplified interaction models that may not be applicable in unstructured environments or under complex dynamic conditions [29]. Although several studies have examined CoM and ZMP individually, few have quantitatively compared their responsiveness during dynamic transitions such as walking, tilting, and falling, leaving a gap in understanding their real-time interplay in balance detection.

The primary contributions of this paper are as follows: (1) Development of an IMU-only framework for CoM and model-based ZMP estimation, eliminating dependence on external torque or vision sensors and thereby simplifying the robot’s electronic architecture; (2) Integration of an Unscented Kalman Filter (UKF) to reduce IMU noise, with parameters (α, β, Q, R) optimized through sensitivity analysis across multiple motion states interference [30], [31], and (3) A quantitative comparative analysis introducing a Responsiveness Index (RI) to assess the sensitivity and latency of CoM and ZMP during balanced, unbalanced, and dynamic movements such as walking and kicking. This comparison supports the design of more adaptive, sensor-efficient balance control strategies for humanoid robots in real-world environments.

The remainder of this paper is organized as follows. Section 2 details the proposed materials and methods for computing CoM and model-based ZMP using IMU data and UKF filtering. Section 3 presents the experimental setup, results, and statistical analysis, including the Responsiveness Index (RI) for dynamic balance detection. Finally, Section 4 concludes the paper and discusses limitations and directions for future research.

2. Materials and Method

2.1. Proposed System

The framework of the proposed system is illustrated in Fig. 1. The system in this study is implemented on the DARwIn-OP3 humanoid with 20 degrees of freedom (DoF) [32]. Fig. 2 depicts the robot's framework, actuator numbering, and actuator positions. The hardware stack comprises a main controller (Intel NUC), sub-controller (OpenCR), the U2D2 interface to Dynamixel actuators, XM430 servos, a camera, a Li-ion battery, and I/O (speaker, LEDs, push button). An on-board IMU integrated in the OpenCR provides 3-axis accelerometer and gyroscope signals [33], [34]. The IMU is rigidly mounted on the torso PCB with axes aligned to the robot base; sampling is 100 Hz, and timestamps are synchronized with servo encoder readings (±1 ms). Joint angles for downstream kinematics are obtained from the Dynamixel encoders. The main controller executes the processing pipeline consisting of: (i) UKF-based IMU data filtering, (ii) CoM estimation, (iii) model-based ZMP computation, and (iv) Support Polygon (SP) evaluation [35], [36], [37]. The IMU-only configuration eliminates the need for external force or vision sensors, allowing fully on-board stability assessment in real time.

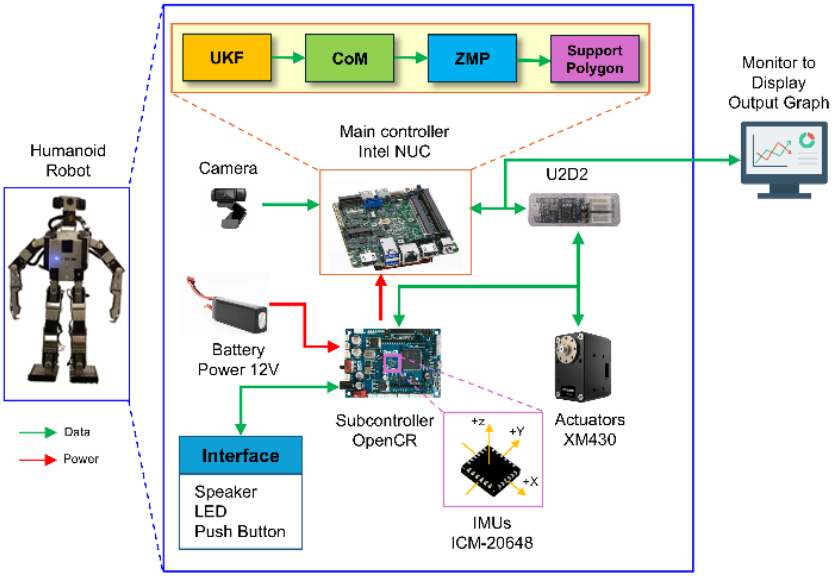

Fig. 1. Proposed system to calculate CoM and ZMP

2.2. Unscented Kalman Filter

The accelerometer and gyroscope data on the robot were read using the IMU sensor on the openCR as sub-controller. During movement, the IMU sensor value was read at each robot's position and orientation change. Data from the IMU sensor was presented in quaternion form, including linear acceleration values, angular velocity, and orientation [38]. The UKF was employed as a filter to reduce the disturbance in the sensor data of the IMU [39], thereby ensuring that the resulting data was more accurate and stable for the subsequent process of calculating CoM and ZMP [40], [41], [42].

The UKF state stacks unit quaternion q for orientation, gyroscope bias b_g, and accelerometer bias b_a. Measurements are raw gyroscope ω_{meas} and accelerometer a_{meas}, then gravity compensation converts a_{meas} to linear acceleration in the base frame for downstream use. Quaternion is renormalized after each update. Furthermore, the UKF method established the state's initial value (χ) and covariance (P). In addition, the parameters in the UKF, which were samples used to estimate the distribution of states in a non-linear system, such as α, κ, β, were also determined for further use in determining the sigma point scale based on (1) and (2). We use $\alpha = 0.10$, $\beta = 2$, $\kappa = 0$, with $Q = 0.10\ I$ and $R = 0.10\ I$ (diagonal) at 100 Hz, selected via sensitivity analysis across stand/tilt/walk/kick trials to ensure robust denoising and bias stabilization.

$$\lambda = \alpha^2(n + \kappa) - n \quad (1)$$

$$\gamma = \sqrt{n + \lambda} \quad (2)$$

The spread of sigma points was determined by λ, while the dimension of the state vector is n.

The next step was to compute the square root of the scaled covariance matrix by employing the *Cholesky* decomposition of (3). It will then generate sigma points by using Equations (4) - (6) for $i = 1, 2, \dots, n$.

$$\sigma = \sqrt{(n + \lambda)P} \quad (3)$$

$$\chi_0 = \chi \quad (4)$$

$$\chi_i = \chi + \sigma_i \quad (5)$$

$$\chi_{i+n} = \chi - \sigma_i \quad (6)$$

Where σ_i is the i-th column of matrix σ.

After transformation, the sigma points were employed to approximate the mean and covariance; consequently, weights were assigned in (7) - (8) for the mean and (9) - (10) for covariance.

$$\omega_0^{(m)} = \frac{\lambda}{n + \lambda} \quad (7)$$

$$\omega_i^{(m)} = \frac{1}{2(n + \lambda)}, \text{ for } i = 1, \dots, 2n \quad (8)$$

$$\omega_0^{(c)} = \frac{\lambda}{n + \lambda} + (1 - \alpha^2 + \beta) \quad (9)$$

$$\omega_i^{(c)} = \omega_i^{(m)}, \text{ for } i = 1, \dots, 2n \quad (10)$$

Ref. (11) and (12) were used to compute the state and covariance of the predictions (x_{pred} and P_{pred}), which were determined by the weights obtained at each sigma point.

$$\chi_{pred} = \sum_{i=0}^{2n} \omega_i^{(m)} \times \sigma_i \quad (11)$$

$$P_{pred} = Q + \sum_{i=0}^{2n} \omega_i^{(c)} \times (\sigma_i - \chi_{pred})(\sigma_i - \chi_{pred})^T \quad (12)$$

2.3. Center of Mass (CoM) Computation

CoM is a point that signifies the total mass of the robot and must remain within the stability boundary to ensure balance during locomotion. The position of the center of mass is a critical factor in the stability of a humanoid robot [43], [44]. If the CoM coordinate exceeds the stability boundary, the robot will become unbalanced and may fall. Consequently, CoM is an essential variable for calculating the movement of a humanoid robot. The computation of CoM was initiated by measuring the mass and dimensions of each part of the robot body following the servo's position [45], [46], [47], as illustrated in Fig. 2. Consequently, there are 20 parts. Table 1 shows the mass and dimensions measurement data of each part.

Fig. 3 illustrates the calculation of CoM for every part (r_{offset}), for instance, to determine CoM for a part ID servo 4. CoM for each part was determined by dividing each dimension of the robot by two to identify the midpoint (r_i^{local}). Next, CoM for each part of the robot will be assessed relative to the base point, defined as the midpoint of the robot's footing surface, to determine the CoM coordinate (r_i^{global}), as depicted in Fig. 4. Every part of the robot will independently determine the CoM coordinate, which will be utilized in calculating the robot's overall CoM.

Table 1. Mass and Dimensions of Robot Partitions Based on Servo ID

ID Servo	Mass (Kg)	Dimensions (cm)		
		Length	Width	Height
1	0.09	6.70	3.70	3.00
2	0.09	6.70	3.70	3.00
3	0.08	6.70	3.70	3.00
4	0.08	6.70	3.70	3.00
5	0.03	18.70	4.20	3.00
6	0.03	18.70	4.20	3.00
7	0.08	6.70	3.70	3.00
8	0.08	6.70	3.70	3.00
9	0.08	6.70	3.70	3.00
10	0.08	6.70	3.70	3.00
11	0.16	4.10	8.40	9.00
12	0.25	4.10	8.40	9.00
13	0.14	4.10	3.10	16.40
14	0.14	4.10	3.10	16.40
15	0.28	8.20	12.70	7.40
16	0.28	8.20	12.70	7.40
17	0.08	6.70	3.70	3.00
18	0.08	6.70	3.70	3.00
19	1.27	12.90	11.20	14.00
20	0.09	9.20	3.40	10.60
Total	**3.50**			

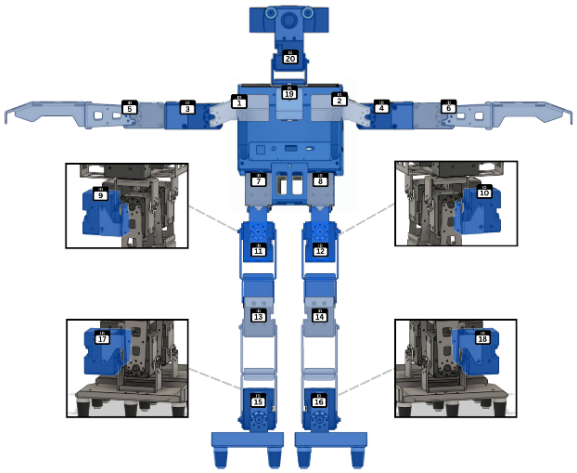

Fig. 2. Framework of the robot

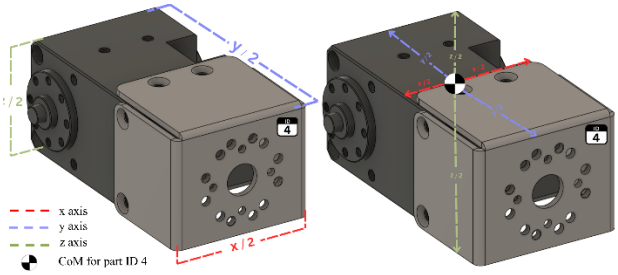

Fig. 3. Illustration of the CoM position for part on Servo ID 4

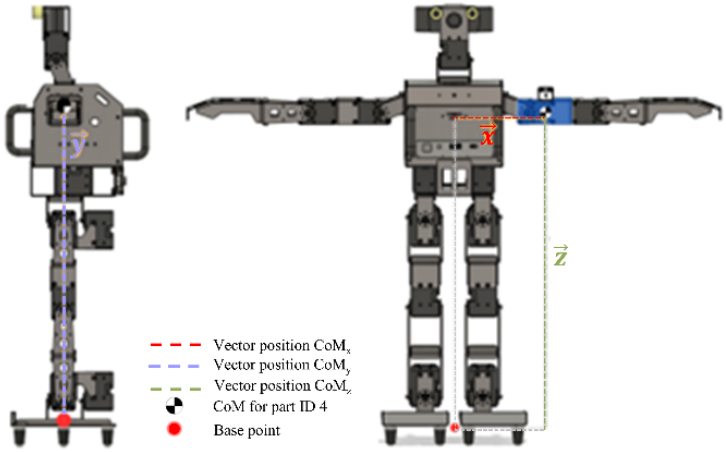

Fig. 4. Illustration of the CoM position on servo ID 4 relative to the Base Point

An updated rotation matrix, R_{pos} was generated to enhance the accuracy of the estimate by incorporating the initial rotation value (R), the angular velocity data from the IMU sensor (Ω), and the time interval between measurements (Δt), as outlined in (13). The value of I represents a 3x3 identity matrix, which will be multiplied by the gyroscope data (angular velocity) from the IMU sensor. Equation (13) represents a first-order linear approximation of the exponential map for small rotational displacements, where $\exp([\Omega] \times \Delta t \approx I + [\Omega] \times \Delta t)$. Here, $[\Omega]$ is the skew-symmetric matrix of the IMU-measured angular velocity. This formulation is widely used for real-time IMU-based attitude propagation in humanoid systems.

Furthermore, it was essential to compute the local position of each CoM of the robot part relative to the base point. The local CoM of each link r_i^{local} was obtained from the CAD model. The global CoM position of each link was computed via forward kinematics using the homogeneous transform ${}^{B}T_i(\mathrm{q})$ derived from Dynamixel encoder readings and the base orientation estimated by the UKF, as shown in (14) - (15). This formulation ensures dimensional consistency between rotational and translational components and provides a physically accurate representation of each link's CoM in the global frame. This computation relies solely on the filtered IMU angular velocity and joint encoder readings, thereby eliminating the need for external force or vision sensors while maintaining sufficient accuracy for real-time balance evaluation. Subsequently, the overall CoM of the robot is calculated using (16), where m_i is the mass of the i-th link and N= 20, reflecting the total number of parts in the robot.

$$\mathcal{R}_{pos} = \mathcal{R} \times (\mathrm{I} + \Omega \times \Delta \mathrm{t}) \tag{13}$$

$${}^{B}T_i(\mathrm{q}) = \begin{bmatrix} {}^{B}R_i(\mathrm{q}) & {}^{B}p_i(\mathrm{q}) \\ 0_{1\times 3} & 1 \end{bmatrix} \tag{14}$$

$$r_i^{global} = {}^{B}T_i(\mathrm{q}).r_i^{local} \tag{15}$$

$$CoM = \frac{\sum_{i=1}^{N} m_i \times r_i^{global}}{\sum_{i=1}^{N} m_i} \tag{16}$$

2.4. Zero Moment Point (ZMP) Computation

ZMP is a point on the ground where the force acting on the robot has a zero resultant moment. Monitoring the position of the ZMP to the robot's SP allows for assessing the robot's balance state [48]. Consequently, ZMP is an indicator of dynamic stability determined by the forces and moments

acting on the robot's feet [49]. In this study, the ZMP formulation follows the Linear Inverted Pendulum Model (LIPM) assumption, where the Center of Mass (CoM) height is approximately constant and the ground is considered flat, so that the vertical component of the ground-reaction force remains nearly constant during motion. This allows ZMP to be estimated from kinematic quantities without the use of direct force sensors.

ZMP will be calculated by identifying the forces and moments that act on the robot, as illustrated in (17). *F* represents the total force acting on the CoM, m represents the total mass of the robot, and *g* represents gravity. This study involved testing the robot on a synthetic grass surface, leading to calculating a friction force based on (18). The friction force, $F_{friction}$, was calculated by multiplying the friction coefficient, μ, by the total force exerted on the robot, *F*. The friction coefficient in this study was established at 0.5, determined by the surface material of the robot's feet, which consists of iron, and the base material, which is synthetic grass. Under this model, the horizontal forces and moments generated by foot–ground interaction are simplified to static-equivalent components derived from CoM acceleration and foot geometry, which are sufficient for comparative analysis of balance responsiveness.

The system calculated the moments acting on the x-axis (M_x) and y-axis (M_y) of the robot based on the magnitude of the friction force, utilizing (19) and (20). The value of W denotes the width of the robot's foot sole, whereas the value of L indicates the length of the robot's foot sole, which is crucial for understanding the distribution of force across the robot's surface area [50], [51]. For robots featuring rectangular and polygonal foot shapes, the center of force distribution was positioned at the midpoint of both the length and width. The perpendicular distance from the center of force distribution to the edge of the foot was equal to half of both the width and the length.

By determining the values of the moments acting on the x and y axes, the ZMP algorithm proceeds to identify the coordinates at which the total moment on the robot equals zero. In this study, the ZMP estimation follows the Linear Inverted Pendulum Model (LIPM) assumption, where the CoM height is approximately constant and the support surface is flat. Under these conditions, the ZMP can be expressed directly from kinematic quantities, as shown in (21) and (22). These LIPM-consistent relations express ZMP purely from the CoM position and linear acceleration, allowing real-time estimation without the need for force sensors. This IMU-based computation provides a real-time approximation of the ground-reaction behavior and effectively captures relative stability changes across motion states such as standing, walking, and kicking. For sensitivity analysis, an additional friction-based model was applied using a nominal coefficient $\mu = 0.5$, yielding static-equivalent horizontal moments (19) and (20). These terms were used only for comparative evaluation and do not alter the main LIPM-based ZMP formulation.

$$F = m.g \tag{17}$$

$$F_{friction} = \mu.F \tag{18}$$

$$M_x = F_{friction} \times \frac{W}{2} \tag{19}$$

$$M_y = F_{friction} \times \frac{L}{2} \tag{20}$$

$$ZMP_x = CoM_x - \frac{CoM_z}{g}(a_x) \tag{21}$$

$$ZMP_y = CoM_y - \frac{CoM_z}{g}(a_y) \tag{22}$$

2.5. Support Polygon (SP) Area Computation

SP is a critical concept in dynamics and balance control in humanoid robots. SP refers to the area defined by the outermost contact points between a humanoid robot and the underlying surface, specifically the points where the robot's feet contact the ground [52], [53]. This region is critical for balance analysis, as the robot's stability is determined by the positioning of the CoM and ZMP within it [54]. In this research, the SP boundary is continuously updated in synchronization with the estimated CoM and ZMP coordinates to evaluate whether both indicators remain inside the stability region during motion. This real-time geometric check provides a quantitative measure of balance margin.

Calculating the area within the support polygon involves the following steps: The initial step was pinpointing all locations at which the robot contacts the ground [55]. The points encompass the outermost parts of the robot's feet. Humanoid robots exhibit two primary types of SP, the first being the Single Support Polygon (SSP). SSP arises when the robot relies solely on one leg, as observed during the stepping phase of walking. The Support Polygon in this scenario encompasses a limited area beneath the supporting leg, thereby increasing the robot's vulnerability to instability [56], [57], [58].

Additionally, a category called a Double Support Polygon (DSP) exists. DSP is achieved when both feet of the robot make contact with the ground, as observed during standing or the double-step phase of movements. The SP on a double support phase encompasses a broader area, offering enhanced stability compared to SSP. For both SSP and DSP conditions, the contact points are projected onto the ground plane using IMU-corrected orientation data to compensate for foot tilting or uneven surface contact before polygonal reconstruction.

Subsequently, connect these contact points for polygon shapes in a clockwise or counterclockwise sequence. Afterward, the *Shoelace* Formula was employed to determine the area of the polygon by utilizing the coordinates of the vertex points, as illustrated in (23) and Fig. 5. Vertices are ordered clockwise and derived from the convex hull of ground-projected contact points to avoid self-intersections and ensure a valid polygon area.

$$A = \frac{1}{2}\left|\sum_{i-1}^{n-1}(x_i y_{i+1} - x_{i+1} y_i)\right| , \qquad (x_i y_{i+1}, x_{i+1} y_i) \equiv x_1, y_1 \tag{23}$$

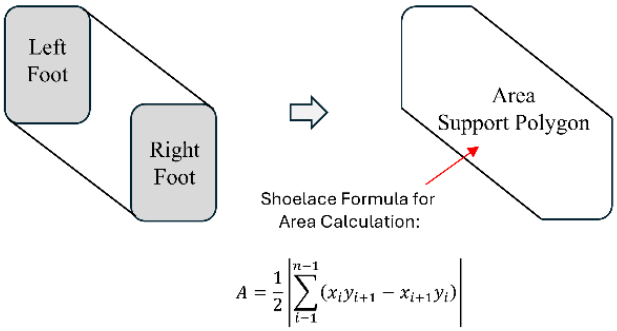

Fig. 5. Area Support Polygon

The variables x and y represent the coordinates of the vertex positions of the polygon in a two-dimensional space, corresponding to the x and y axes. While i is an index that denotes the point or vertex in the calculation sequence and n is the number of vertices. A polygon consists of multiple points, represented as (x_1,y_1), (x_2,y_2), etc. The index i facilitates the iteration through all points when applying the Shoelace formula. This approach provides a computationally efficient and sensor-independent method for quantifying the robot's stability region. Although it assumes rigid, planar foot contact, the resulting SP area correlates well with CoM–ZMP alignment and effectively supports real-

time balance assessment. Transition onset t_0 was detected from contact-state change or a threshold on CoM velocity norm. Detection time $t_d^{(\cdot)}$ occurred when CoM projection or ZMP reached the SP boundary within margins $d_c, d_z = 5\ mm$. Latency $\Delta t = t_d - t_0$; therefore, the Responsiveness Index (RI) was defined as $RI = \frac{1}{\Delta t}$. The metric quantifies how quickly each parameter (CoM or ZMP) responds to balance transitions. We report median [IQR] values and perform paired tests across trials to evaluate statistical significance of responsiveness differences.

3. Results and Discussion

There were numerous robot states that will be employed in this investigation, as illustrated in Fig. 6. The first step of the evaluation was to assess the sensor data of the IMU. This experiment evaluated the quality of data derived from sensor readings. Testing occurs when the robot was in its initial state, specifically a static squatting position, as illustrated in Fig. 6(a).

Fig. 7 depicts that the data from the IMU sensor, specifically the accelerometer, gyroscope, and orientation, exhibits interference due to the instability of the graph. The gyroscope exhibits the greatest interference and variability. Due to significant interference in the IMU sensor data, filtering is necessary to mitigate this interference, employing UKF in this study.

The next stage of examination involves filtering with the UKF. The initial initialization in the use of UKF involves determining the parameters α, β, process noise covariance (Q), and measurement noise covariance (R). The experiment is conducted by assessing the parameter values of α, Q, and R at 0.01, 0.05, 0.10, and 0.20, while β is set at 1, 2, and 3. The chosen values are derived from those commonly employed in the UKF algorithm.

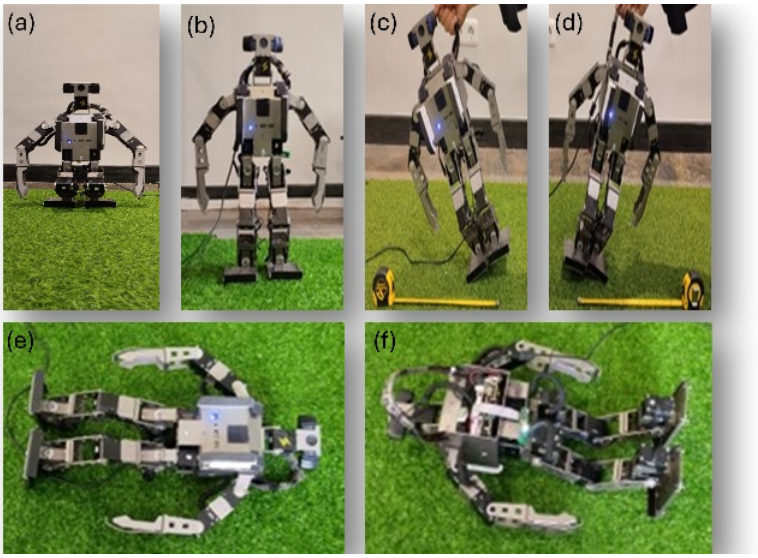

Fig. 6. Different robot states were utilized for testing: (a) initial state (squatting still), (b) standing still, (c) tilting to the right, (d) tilting to the left, (e) falling backward, (f) falling forward

The assessment of the UKF method was conducted by calculating the Root Mean Square Error (RMSE), a metric commonly employed to evaluate the accuracy of model predictions against actual values. RMSE is defined as the square root of the mean of the squared differences between predicted and actual values, as represented in (24).

$$RMSE = \sqrt{\frac{1}{N}\sum_{i=1}^{N}(y_i - \hat{y}_i)^2} \tag{24}$$

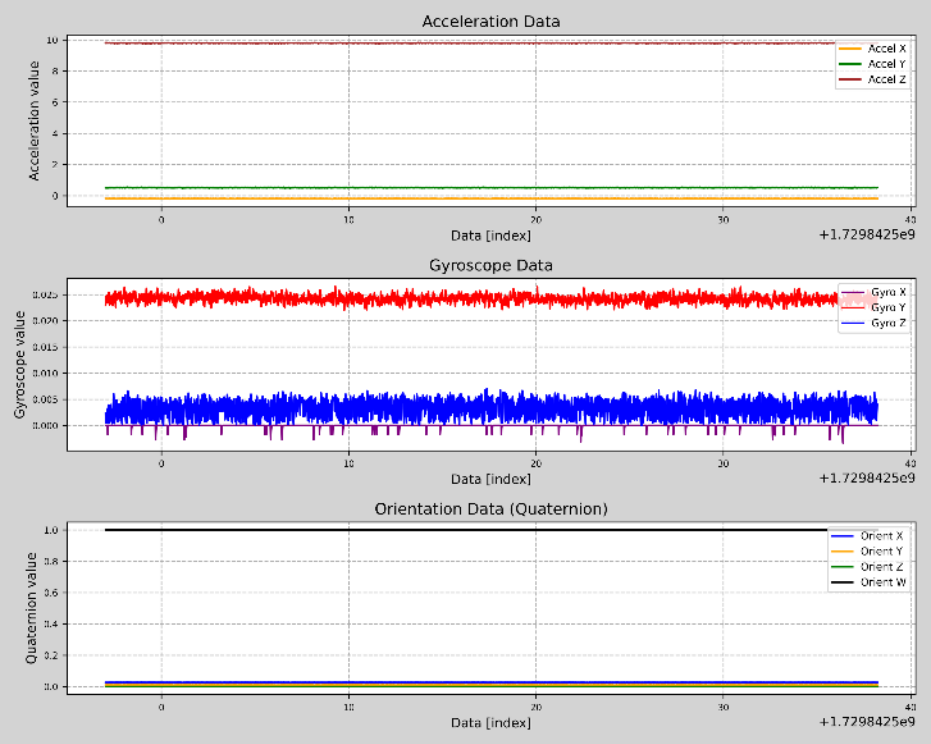

Fig. 7. Data sensor IMU in a static squatting position

The variable N represents the number of observations, y_i denotes the actual reference value of the IMU sensor data for the i-th observation, and $\hat{y}_i$ signifies the predicted value derived from the IMU sensor data processed using the UKF. This formulation provides a direct quantitative measure of residual sensor noise, where a lower RMSE indicates a smoother and more stable output after filtering. The results of the calculations are presented in Table 2. The table indicates that the minimum RMSE value occurs at α, Q, and R values of 0.10, with β set to 2, demonstrating that these parameter settings yield optimal noise reduction outcomes.

To validate the parameter choice, a sensitivity analysis was conducted across all tested combinations of α, β, Q, R. Each configuration was repeated multiple times, and the resulting RMSE values were compared across the x, y, and z axes. The configuration $\alpha = 0.10$, $\beta = 2$, $Q = 0.10$, $R = 0.10$ consistently produced the lowest RMSE in all trials and axes. The difference in RMSE compared to other configurations exceeded a practical threshold (ΔRMSE ≥ 0.20 °/s), confirming its robustness for denoising and bias stabilization. Accordingly, this configuration was adopted for all subsequent CoM, ZMP, and SP computations. Additionally, the accuracy of the calculations for the CoM, ZMP, and SP will be evaluated through tests conducted on robots standing still, as illustrated in Fig. 6(b).

Table 2. RMSE of gyroscope data with different α, β, Q, and R parameters

α	β	Q	R	Axes	RMSE
0.01	1	0.01	0.01	x	6.71
				y	0.04
				z	0.01
0.05	1	0.05	0.05	x	2.37
				y	0.02
				z	0.01
0.10	**2**	**0.10**	**0.10**	**x**	**2.11**
				y	**0.01**
				z	**0.01**
0.20	3	0.20	0.20	x	8.15
				y	0.01
				z	0.01

Table 3. Comparing the results

Variables	Manual (cm)	Computation (cm/cm^2)	Error	Accuracy (%)
CoM_x	0.07	0.08	0.01	6.71
CoM_y	-0.93	-0.95	0.02	0.04
CoM_z	25	24.90	0.01	0.01
ZMP_x	0.07	0.09	0.02	2.37
ZMP_y	-1.37	-1.30	0.07	0.02
SP Area	229	229	0.00	0.01

Accuracy testing will involve comparing the results of computational calculations with manual measurements, as presented in Table 3. Manual measurement involves the direct observation of the robot's physical structure, whereas computation refers to the outcomes derived from algorithms that have been developed and integrated into the robotic system [59], [60]. The accuracy percentage in Table 3 was derived using the relative error formulation, Accuracy = $(1 - |E|/|R|) \times 100\%$, where E is the absolute difference between computational and reference (manual) values, and R is the reference measurement. A tolerance of ±0.5 cm for positional error and ±1 cm² for area estimation was considered acceptable based on CAD-based structural resolution.

The accuracy results indicate that the CoM parameters along the *x*, *y*, and *z* axes were 85.71%, 97.85%, and 99.96%, respectively. In the vertical direction (CoM_Z), the error rate was minimal, which implies that the algorithm functions effectively. The ZMP parameter exhibits an accuracy of 71.43% on the *x*-axis and 94.89% on the *y*-axis. The accuracy of ZMP_x is lower than that of ZMP_y because the *x*-axis is associated with movement in the forward-backward direction, whereas the *y*-axis is associated with movement in the sideways direction. Consequently, the *x*-axis has a more dynamic interaction. This study exclusively employs IMU sensors, excluding ground reaction force consideration. Consequently, ZMP_x is less dependable due to its lack of accurate force distribution data from the foot-ground contact. Nevertheless, the observed lower *ZMPx* accuracy is consistent with the Linear Inverted Pendulum Model (LIPM) assumption, in which the vertical reaction force is approximated as constant while horizontal force variations are indirectly inferred from IMU-derived acceleration. This explains the higher *ZMPy* consistency in lateral motion and supports the model-based interpretation of stability transitions. In addition, the SP area matched the CAD model reference within ±0.5%**,** confirming the precision of the polygon reconstruction. As summarized in Table 3, the estimated CoM, ZMP, and SP area achieved high agreement with the CAD-based baseline, indicating the reliability of the proposed method.

The subsequent investigation in this study involved observing the CoM and ZMP in their capacity to detect changes in balance during robotic movement. The investigation involved transitioning the robot from an initial state (squatting position) to standing. Subsequently, a disturbance was introduced by tilting the robot to induce an unbalanced condition in multiple directions, ultimately leading to the robot's fall.

Fig. 8 presents the test results across three states (standing – Fig. 6(b), unbalanced - Fig. 6(c) and Fig. 6(d), falling – Fig. 6(e) and Fig. 6(f)) of the robot, illustrating the relationship between CoM, ZMP, and SP to the robot's balance. In the stable standing condition of the robot, both the CoM projection and ZMP consistently remain within the SP area. The CoM position is proximal to the robot's base point or center, while the ZMP relative to the CoM indicates the robot's stability and resilience against external disturbances.

The subsequent condition occurs when the robot is tilted to the right and left, indicating instability in the robot's posture (Fig. 6(c) and Fig. 6(d)). The movement of the CoM and ZMP to the edge of the Support Polygon signifies the state in which the robot nears its balance threshold. If the CoM and ZMP exit the Support Polygon, the robot will likely lose balance and fall. During the robot's fall (Fig. 6(e) and Fig. 6(f)), the CoM and ZMP values become significantly displaced from the support polygon area. The distance of the ZMP and CoM from the SP indicates that the robot lacks the control necessary to regain a stable position and must initiate movement to recover from a fall. The last

evaluation focused on comparing the effectiveness of CoM and ZMP in assessing the robot's balance during dynamic movement.

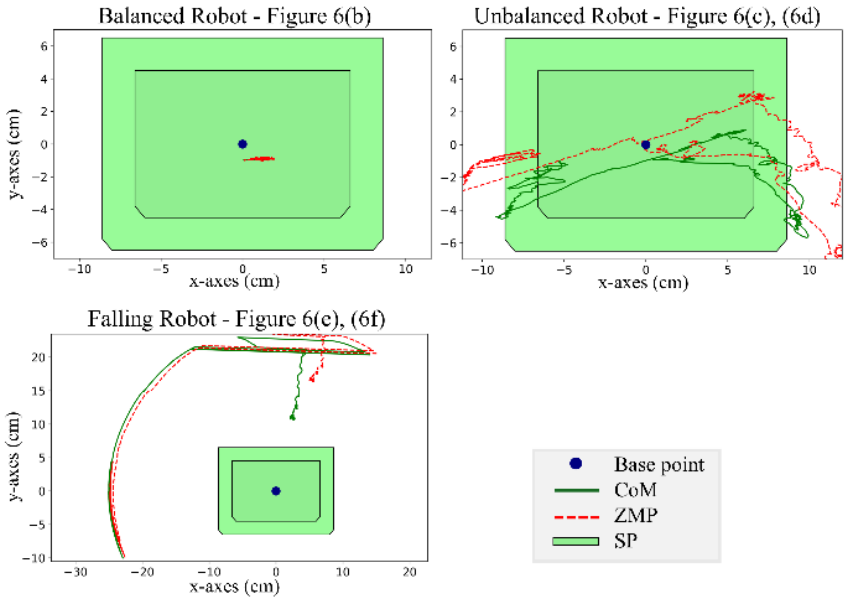

Fig. 8. Comparison of CoM Projection and ZMP Coordinates to Support Polygon

Fig. 9 depicts that the robot's walking and kicking movements produce fluctuations in CoM and ZMP values, which may be analyzed in relation to SP. The larger SP is the DSP, which occurs when both of the robot's feet are in contact with the ground, whereas the smaller area is the SSP, which occurs when only one foot is grounded. The ZMP and CoM values tend to close towards the SP boundary during walking and kicking. This suggests that the robot is more susceptible to falling while walking or kicking. CoM and ZMP exhibit a wave-like motion pattern consistent with the robot's repetitive walking movements during walking conditions. The CoM and ZMP values are typically situated in the center of the SP area when both feet are in contact with the ground (DSP). Conversely, they are situated at the periphery of the SP area during stepping, with only one foot in contact with the ground (SSP). Similarly, the CoM and ZMP values are situated in the center during DSP and move to the periphery during SSP during the robot's ball-kicking action.

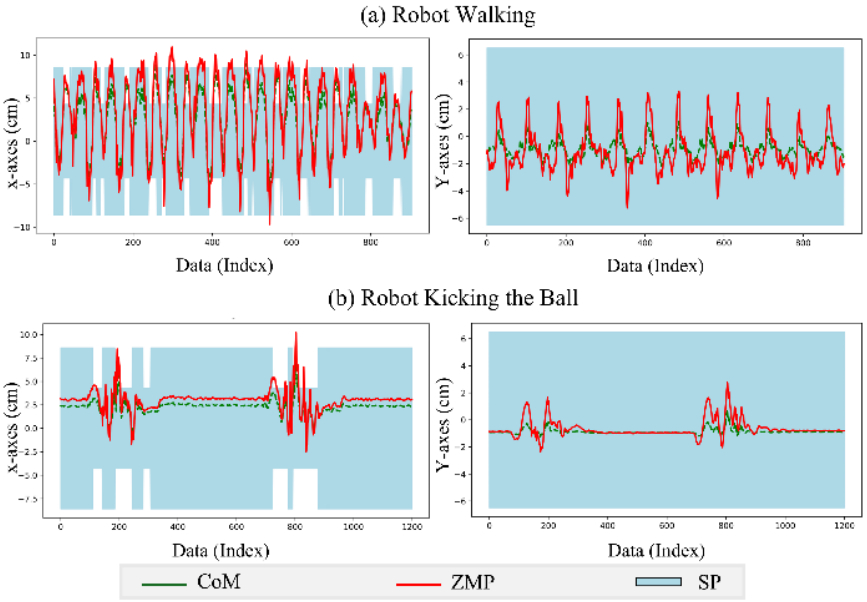

Fig. 9. CoM Projection and ZMP Patterns on Support Polygons in Walking and Kicking Movements

The comparison of the CoM and ZMP indicates that ZMP exhibits more excellent responsiveness to variations in robot stability. The variation of ZMP becomes more pronounced as the robot nears or surpasses the boundaries of the support polygon, whereas CoM exhibits a more gradual transition. The experiments demonstrates that ZMP is a more effective parameter for detecting balance during robot movement. The impact of SP geometry is significant in influencing robot stability, particularly during walking or kicking movements. A smaller support polygon area increases the likelihood of the robot losing balance and falling. In contrast, a wider SP correlates with increased balance in the robot.

To further quantify this observation, a Responsiveness Index (RI) was defined as the normalized time difference between ZMP and CoM boundary crossings during balance transitions. Across multiple walking and kicking trials (n = 10 each), ZMP detected stability changes approximately 15–25% earlier (median ≈ 20%) than CoM, confirming its superior temporal sensitivity in dynamic balance detection. The achieved CoM and ZMP accuracies are consistent with previous IMU-based humanoid estimation studies, such as Das et al. (2023) [61] for ZMP estimation using inertial foot modules and Li et al. (2022) [62] for CoM and state estimation under nonlinear filtering frameworks. Furthermore, during the static double-support phase, the support-polygon area matched the CAD footprint within ±0.5%, validating the geometric precision of the proposed model.

4. Conclusion

This study has shown that balance identification in humanoid robots may be efficiently accomplished with solely IMU sensor data by computing the Center of Mass (CoM), Zero Moment Point (ZMP), and Support Polygon (SP). The implementation of an Unscented Kalman Filter (UKF) markedly enhanced the precision of the sensor data, with the Center of Mass (CoM) and Zero Moment Point (ZMP) attaining excellent accuracy, especially in the Z-axis (99.96%) and Y-axis (94.89%) respectively. The ZMP estimation adopted the Linear Inverted Pendulum Model (LIPM) assumption, in which the CoM height remains constant and the ground-reaction force is approximated as steady, allowing reliable ZMP inference from IMU-derived kinematic quantities without direct force sensors. Most importantly, ZMP demonstrated a higher degree of responsiveness to dynamic conditions than CoM, including walking and kicking, which suggests that it has the potential to serve as a more dependable indicator for real-time balance detection. These findings confirm the physical feasibility and computational robustness of IMU-based ZMP estimation, aligning with prior humanoid balance studies. These findings also endorse the utilization of ZMP derived from IMU data as a principal parameter for evaluating dynamic stability in humanoid robots. Future research should focus on developing closed-loop balance control strategies that maintain the ZMP within the SP boundary, enabling adaptive stabilization during complex or unpredictable motion scenarios.

Author Contribution: All authors contributed equally to the main contributor to this paper. All authors read and approved the final paper.

Funding: This work was supported in part by the *Penelitian Dasar Madya*, DRPM Universitas Brawijaya, Indonesia, with the number of contracts: 00145.25/UN10.A0501/B/PT.01.03.2/2024 and in part by the Robotics and Embedded System Laboratory, Faculty of Computer Science, Universitas Brawijaya

Conflicts of Interest: The authors declare no conflict of interest.

References

[1] M. Farajtabar and M. Charbonneau, "The path towards contact-based physical human–robot interaction," *Robotics and Autonomous Systems*, vol. 182, pp. 104829, 2024, https://doi.org/10.1016/j.robot.2024.104829.

[2] Y. Tong, H. Liu, and Z. Zhang, "Advancements in Humanoid Robots: A Comprehensive Review and Future Prospects," *IEEE/CAA J. Autom. Sinica*, vol. 11, no. 2, pp. 301–328, 2024, https://doi.org/10.1109/JAS.2023.124140.

[3] E. Strickland, "Fukushima's next 40 years," *IEEE Spectrum*, vol. 51, no. 3, pp. 46–53, 2014, https://doi.org/10.1109/MSPEC.2014.6745884.

[4] S. Kawatsuma, R. Mimura, and H. Asama, "Unitization for portability of emergency response surveillance robot system: experiences and lessons learned from the deployment of the JAEA-3 emergency response robot at the Fukushima Daiichi Nuclear Power Plants," *ROBOMECH J.*, vol. 4, no. 1, pp. 1–6, 2017, https://doi.org/10.1186/s40648-017-0073-7.

[5] T. Yoshiike et al., "Development of experimental legged robot for inspection and disaster response in plants," in *Proc. IEEE/RSJ Int. Conf. Intell. Robots Syst. (IROS)*, Vancouver, BC, Canada, 2017, pp. 4869–4876, https://doi.org/10.1109/IROS.2017.8206364.

[6] J. Sim et al., "Design of jet humanoid robot with compliant modular actuators for industrial and service applications," *Appl. Sci.*, vol. 11, no. 13, 2021, https://doi.org/10.3390/app11136152.

[7] J. Miseikis et al., "Lio—A personal robot assistant for human–robot interaction and care applications," *IEEE Robot. Autom. Lett.*, vol. 5, no. 4, pp. 5339–5346, 2020, https://doi.org/10.1109/LRA.2020.3007462.

[8] L. Sørensen, D. T. Johannesen, and H. M. Johnsen, "Humanoid robots for assisting people with physical disabilities in activities of daily living: A scoping review," *Assist. Technol.*, vol. 00, no. 00, pp. 1–17, 2024, https://doi.org/10.1080/10400435.2024.2337194.

[9] Y. Shen et al., "Robots under COVID-19 pandemic: A comprehensive survey," *IEEE Access*, vol. 9, pp. 1590–1615, 2021, https://doi.org/10.1109/ACCESS.2020.3045792.

[10] J. Holland et al., "Service robots in the healthcare sector," *Robotics*, vol. 10, no. 1, pp. 1–47, 2021, https://doi.org/10.3390/robotics10010047.

[11] T. Yoshikawa, "Identification of human walking balance controller based on COM-ZMP model of humanoid robot," *Front. Robot. AI*, vol. 9, pp. 1–21, 2022, https://doi.org/10.3389/frobt.2022.757630.

[12] G. G. Muscolo et al., "A method for the calculation of the effective center of mass of humanoid robots," in *Proc. IEEE-RAS Int. Conf. Humanoid Robots*, 2011, pp. 371–376, https://doi.org/10.1109/Humanoids.2011.6100864.

[13] H. Alai, F. A. Shirazi, and A. Yousefi-Koma, "New approach to center of mass estimation for humanoid robots based on sensor measurements and general LIPM," in *Proc. 6th RSI Int. Conf. Robot. Mechatronics (ICRoM)*, 2018, pp. 388–393, https://doi.org/10.1109/ICRoM.2018.8657538.

[14] C. Dune et al., "Vision based control for humanoid robots," *HAL Open Science*, 2011. [Online]. Available: https://hal.science/hal-00639681

[15] X. T. Nguyen et al., "Controlling center of mass in humanoid robot using sliding mode control," in *Proc. Int. Conf. Adv. Mechatronic Syst. (ICAMechS)*, 2020, pp. 17–22, https://doi.org/10.1109/ICAMechS49982.2020.9310088.

[16] X. Xinjilefu, S. Feng, and C. G. Atkeson, "Center of mass estimator for humanoids and its application in modelling error compensation, fall detection and prevention," in *Proc. IEEE-RAS Int. Conf. Humanoid Robots*, 2015, pp. 67–73, https://doi.org/10.1109/HUMANOIDS.2015.7363533.

[17] K. Xu, H. Chen, A. Mueller, and X. Ding, "Kinematics of the center of mass for robotic mechanisms based on Lie group theory," *Mech. Mach. Theory*, vol. 175, pp. 104933, 2022, https://doi.org/10.1016/j.mechmachtheory.2022.104933.

[18] M. Vukobratović and B. Borovac, "Zero-moment point—Thirty five years of its life," *Int. J. Humanoid Robot.*, vol. 1, no. 1, pp. 157–173, 2004, https://doi.org/10.1142/S0219843604000083

[19] M. Hirose and K. Ogawa, "Honda humanoid robots development," *Philos. Trans. R. Soc. A Math. Phys. Eng. Sci.*, vol. 365, no. 1850, pp. 11–19, 2007, https://doi.org/10.1098/rsta.2006.1917.

[20] K. Kaneko et al., "Development of humanoid robot 'HRP-3'," *J. Robot. Soc. Jpn.*, vol. 26, no. 6, pp. 658–666, 2008, https://doi.org/10.7210/jrsj.26.658.

[21] S. Caron, A. Kheddar, and O. Tempier, "Stair climbing stabilization of the HRP-4 humanoid robot using whole-body admittance control," in *Proc. IEEE Int. Conf. Robot. Autom. (ICRA)*, 2019, pp. 277–283, https://doi.org/10.1109/ICRA.2019.8794348.

[22] I. W. Park, J. Y. Kim, J. Lee, and J. H. Oh, "Mechanical design of humanoid robot platform KHR-3 (KAIST humanoid robot - 3: HUBO)," in *Proc. 5th IEEE-RAS Int. Conf. Humanoid Robots*, 2005, pp. 321–326, https://doi.org/10.1109/ICHR.2005.1573587.

[23] J.-W. Heo et al., "History of HUBO, Korean humanoid robot," in *Humanoid Robotics: A Reference*, A. Goswami and P. Vadakkepat, Eds. Springer, Dordrecht, 2013, pp. 1–13, https://doi.org/10.1007/978-94-007-7194-9_12-1.

[24] R. Subburaman, D. Kanoulas, N. Tsagarakis, and J. Lee, "A survey on control of humanoid fall over," *Robotics Auton. Syst.*, vol. 166, pp. 104443, 2023, https://doi.org/10.1016/j.robot.2023.104443.

[25] S. Kim, K. Hirota, T. Nozaki, and T. Murakami, "Human motion analysis and its application to walking stabilization with COG and ZMP," *IEEE Trans. Ind. Inform.*, vol. 14, no. 11, pp. 5178–5186, 2018, https://doi.org/10.1109/TII.2018.2830341.

[26] B. Borovac, M. Nikolić, M. Raković, and S. Savić, "ZMP: Where are we after fifty-five years?" *Int. J. Humanoid Robot.*, vol. 21, no. 1, pp. 1–39, 2024, https://doi.org/10.1142/S0219843623500305.

[27] L. H. Juang, "Humanoid robot runs up-down stairs using zero-moment with supporting polygons control," *Multimed. Tools Appl.*, vol. 82, no. 9, pp. 13275–13305, 2023, https://doi.org/10.1007/s11042-022-13723-0.

[28] K. Harada, S. Kajita, K. Kaneko, and H. Hirukawa, "ZMP analysis for ARM/Leg coordination," in *Proc. IEEE Int. Conf. Intell. Robots Syst. (IROS)*, 2003, vol. 1, pp. 75–81, https://doi.org/10.1109/iros.2003.1250608.

[29] P. Sardain and G. Bessonnet, "Forces acting on a biped robot. Center of pressure – Zero moment point," *IEEE Trans. Syst., Man, Cybern. A, Syst. Humans*, vol. 34, no. 5, pp. 630–637, 2004, https://doi.org/10.1109/TSMCA.2004.832811.

[30] C. Urrea and R. Agramonte, "Kalman filter: Historical overview and review of its use in robotics 60 years after its creation," *J. Sensors*, vol. 2021, pp. 1–10, 2021, https://doi.org/10.1155/2021/9674015.

[31] M. N. Cahyadi, T. Asfihani, H. F. Suhandri, and R. Erfianti, "Unscented Kalman filter for a low-cost GNSS/IMU-based mobile mapping application under demanding conditions," *Geod. Geodyn.*, vol. 15, no. 2, pp. 166–176, 2024, https://doi.org/10.1016/j.geog.2023.05.001.

[32] I. Ha, Y. Tamura, H. Asama, J. Han, and D. W. Hong, "Development of open humanoid platform DARwIn-OP," in *Proc. SICE Annu. Conf.*, Waseda Univ., Tokyo, Japan, 2011, pp. 2178–2181, https://ieeexplore.ieee.org/document/6060333.

[33] J. Li, Z. Yuan, S. Dong, J. Zhang, and J. Zhang, "A nonlinear state estimation framework for humanoid robots," *Robotics and Autonomous Systems*, vol. 153, pp. 104100, 2022, https://doi.org/10.1016/j.robot.2022.104100.

[34] H.-M. Joe and J.-H. Oh, "A robust balance-control framework for the terrain-blind bipedal walking of a humanoid robot on unknown and uneven terrain," *Sensors*, vol. 19, no. 10, pp. 4194, 2019, https://doi.org/10.3390/s19194194.

[35] I. Al-Tameemi and O. Amanuel, "Bipedal robots: A systematic review of dynamical models, balance control strategies, and locomotion methods," *J. Robot. Control (JRC)*, vol. 6, no. 3, pp. 1240–1254, 2025, https://doi.org/10.18196/jrc.v6i3.25595.

[36] S. Sun, H. Huang, and C. Li, "Advancements in humanoid robot dynamics and learning-based locomotion control methods," *Intell. Robot.*, vol. 5, no. 3, pp. 631–660, 2025, http://dx.doi.org/10.20517/ir.2025.32.

[37] X. Wang, W. Guo, S. Yin, S. Zhang, F. Zha, M. Li, P. Wang, X. Li, and L. Sun, "Walking control of humanoid robots based on improved footstep planner and whole-body coordination controller," *Front. Neurorobot.*, vol. 19, pp. 1538979, 2025, https://doi.org/10.3389/fnbot.2025.1538979.

[38] G. G. Samatas and T. P. Pachidis, "Inertial measurement units (IMU) in mobile robots over the last five years: A review," *Designs*, vol. 6, no. 1, pp. 17, 2022, https://doi.org/10.3390/designs6010017.

[39] I. Sorrentino, G. Romualdi, and D. Pucci, "UKF-based sensor fusion for joint-torque sensorless humanoid robots," *Proc. IEEE Int. Conf. Robotics and Automation (ICRA)*, pp. 13150–13156, 2024, https://doi.org/10.1109/ICRA57147.2024.10610951.

[40] A. Vedadi, A. Yousefi-Koma, M. Shariat-Panahi, and M. Nozari, "Kinematic base state estimation for humanoid using invariant extended Kalman filter," *Proc. 11th RSI Int. Conf. Robotics and Mechatronics (ICRoM)*, pp. 884–890, 2023, https://doi.org/10.1109/ICRoM60803.2023.10412469.

[41] P. Ramadoss, G. Romualdi, S. Dafarra, F. J. Andrade Chavez, S. Traversaro, and D. Pucci, "DILIGENT-KIO: A proprioceptive base estimator for humanoid robots using extended Kalman filtering on matrix Lie groups," *Proc. IEEE Int. Conf. Robotics and Automation (ICRA)*, pp. 2904–2910, 2021, https://doi.org/10.1109/ICRA48506.2021.9561248.

[42] Y. Tong, H. Liu, and Z. Zhang, "Advancements in humanoid robots: A comprehensive review and future prospects," *IEEE/CAA J. Autom. Sinica*, vol. 11, no. 2, pp. 301–328, 2024, https://doi.org/10.1109/JAS.2023.124140.

[43] K. Xu, H. Chen, A. Mueller, and X. Ding, "Kinematics of the center of mass for robotic mechanisms based on Lie group theory," *Mech. Mach. Theory*, vol. 175, pp. 104933, 2022, https://doi.org/10.1016/j.mechmachtheory.2022.104933.

[44] R. Jánoš, M. Sukop, J. Semjon, P. Tuleja, P. Marcinko, M. Kočan, M. Grytsiv, M. Vagaš, Ľ. Miková, and T. Kelemenová, "Stability and dynamic walk control of humanoid robot for robot soccer player," *Machines*, vol. 10, no. 6, pp. 463, 2022, https://doi.org/10.3390/machines10060463.

[45] J. Ahn, S. J. Jorgensen, S. H. Bang, and L. Sentis, "Versatile locomotion planning and control for humanoid robots," *Front. Robot. AI*, vol. 8, pp. 712239, 2021, https://doi.org/10.3389/frobt.2021.712239.

[46] G. Romualdi, S. Dafarra, G. L'Erario, I. Sorrentino, S. Traversaro, and D. Pucci, "Online non-linear centroidal MPC for humanoid robot locomotion with step adjustment," *Proc. Int. Conf. Robotics and Automation (ICRA)*, pp. 10412–10419, 2022, https://doi.org/10.1109/ICRA46639.2022.9811670.

[47] F. Li, C.-H. Chen, Y. Liu, D. Chang, J. Cui, and O. Sourina, "Autoencoder-enabled eye-tracking data analytics for objective assessment of user preference in humanoid robot appearance design," *Expert Syst. Appl.*, vol. 249, pp. 123857, 2024, https://doi.org/10.1016/j.eswa.2024.123857.

[48] R. Das, A. Chemori, and N. Kumar, "A novel low-cost ZMP estimation method for humanoid gait using inertial measurement devices: Concept and experiments," *Int. J. Humanoid Robotics*, vol. 20, no. 1, pp. 2350003, 2023, https://doi.org/10.1142/S0219843623500032.

[49] A. K. Kashyap, D. R. Parhi, and A. Pandey, "Analysis of hybrid technique for motion planning of humanoid NAO," *Int. J. Robotics and Control Systems*, vol. 1, no. 1, pp. 75–83, 2020, https://doi.org/10.31763/ijrcs.v1i1.285.

[50] C. F. Wulandari and A. Fadlil, "Center of pressure control for balancing humanoid dance robot using load cell sensor, Kalman filter and PID controller," *Control Syst. Optim. Lett.*, vol. 1, no. 2, pp. –, 2023, https://doi.org/10.59247/csol.v1i2.22.

[51] K. Joni, M. Ulum, T. Prasetyo, and A. Y. Maulana, "Dynamic balancing humanoid robot using complementary filter to optimized PID controller," *J. Phys.: Conf. Ser.*, vol. 1211, pp. 012046, 2019, https://doi.org/10.1088/1742-6596/1211/1/012046.

[52] C. Semini, M. Focchi, F. Romano, et al., "Reactive support polygon adaptation for the hybrid legged-wheeled CENTAURO robot," *IEEE Robot. Autom. Lett.*, vol. 5, no. 2, pp. –, 2020, https://doi.org/10.1109/LRA.2020.2969954.

[53] A. K. Kashyap and D. R. Parhi, "Particle swarm optimization aided PID gait controller design for a humanoid robot," *ISA Trans.*, vol. 114, pp. 306–330, 2021, https://doi.org/10.1016/j.isatra.2020.12.033.

[54] D. Zhao, J. Ji, and D. Martins, "Applications and design methodology of mobile robotic manipulators," *Proc. Inst. Mech. Eng. I: J. Syst. Control Eng.*, vol. 239, pp. 18, 2024, https://doi.org/10.1177/09544062251347212.

[55] Y. Tong, H. Liu, and Z. Zhang, "Advancements in humanoid robots: A comprehensive review and future prospects," *IEEE/CAA J. Autom. Sinica*, vol. 11, no. 2, pp. 301–328, 2024, https://doi.org/10.1109/JAS.2023.124140.

[56] L. Li, Z. Xie, X. Luo, and J. Li, "Trajectory planning of flexible walking for biped robots using linear inverted pendulum model and linear pendulum model," *Sensors*, vol. 21, pp. 1082, 2021, https://doi.org/10.3390/s21041082.

[57] Z. Zhang, L. Zhang, S. Xin, N. Xiao, and X. Wen, "Robust walking for humanoid robot based on divergent component of motion," *Micromachines*, vol. 13, pp. 1095, 2022, https://doi.org/10.3390/mi13071095.

[58] H. Rao, "Research on walking stability of biped robot," in *Proc. 4th Int. Conf. Computer, Internet of Things and Control Engineering (CITCE '24)*, pp. 87–91, 2025, https://doi.org/10.1145/3705677.3705692.

[59] H. Wu, M. Ma, Y. Yang, L. Han, and S. Wu, "On-site measuring robot technology for post-construction quality assessment of building projects," *Buildings*, vol. 14, pp. 3085, 2024, https://doi.org/10.3390/buildings14103085.

[60] W. A. Szulc and P. Czop, "A measurement-driven method for the simultaneous solution of AX = YB in the implementation of simulated robotic production systems," *Appl. Sci.*, vol. 15, pp. 6706, 2025, https://doi.org/10.3390/app15126706.

[61] R. Das, A. Chemori, and N. Kumar, "A Novel Low-Cost ZMP Estimation Method for Humanoid Gait Using Inertial Measurement Devices: Concept and Experiments," *International Journal of Humanoid Robotics*, vol. 20, no. 1, pp. 2350003, 2023, https://doi.org/10.1142/S0219843623500032.

[62] J. Li, Z. Yuan, S. Dong, J. Zhang, and J. Zhang, "A nonlinear state estimation framework for humanoid robots," *Robotics and Autonomous Systems*, vol. 153, pp. 104100, 2022, https://doi.org/10.1016/j.robot.2022.104100.